International Journal for Housing Science and Its Applications
Publish August 10, 2025. Volume 46, Issue 4 Pages 5661-5671

https://doi.org/10.70517/ijhsa464406

Research on Measurement and Analysis Methods for Non-Contact Aircraft Landing Impact Tests

Zhaoming Huang[1,2,*], Rui Hu[1] and Chenchen Zhu[1,2]
[1] Aircraft Strength Research Institute of China, Xi'an, Shaanxi, 710000, China
[2] National Key Laboratory of Strength and Structural Integrity, Xi'an, Shaanxi, 710000, China
Corresponding authors: (e-mail: hzmhzm14@qq.com).

Abstract Aircraft landing safety assessment has become a key technical challenge in the development of modern aviation industry. The traditional contact measurement method has problems such as sensor damage and limited measurement accuracy under high-impact environment, which makes it difficult to accurately obtain the spatial attitude and structural deformation information of the airplane at the moment of landing. The non-contact measurement technology, with its advantages of high precision and real-time, provides a new idea to solve this technical challenge. This paper proposes a non-contact measurement technology based on the aircraft landing impact test space attitude and deformation measurement and analysis method. The research adopts the modal superposition method to establish a large spreading ratio elastic aircraft dynamics model, and combines the fluid cavity unit and the viscous hyperelasticity intrinsic model to construct a three-dimensional finite element model of the aviation tire. ABAQUS software is used to simulate and analyze the impact response of tires under different landing load conditions, and to study the deformation characteristics and stress distribution law during the landing process. The results show that the tire compression rate reaches 44.86% when the landing load is 273160N, and the grounded area is 148169mm²; the impact spectrum analysis shows that the acceleration amplification coefficient reaches the maximum value of 6.2 at 507Hz; when the aircraft sink rate is 2.5m/s, the peak of the tread pressure is 13.41MPa, and the deformation amount of the tire is 0.154m. Safety analysis the results show that the aircraft can land safely under the condition of sink rate of 1.0m/s, and the peak contact force of the tire is 325460N, which does not exceed the maximum load of 379636 N. This method provides an effective measurement and analysis means for the impact test of aircraft landing, which is of great significance to improve the safety of aircraft landing.

Index Terms Non-contact measurement, aircraft landing impact, space attitude, deformation measurement, finite element analysis, aviation tire

I. Introduction

The scale of China's general aviation airports still has a large gap compared with other aviation developed countries, especially in the remote areas of central and western regions with serious lack of coverage of feeder airports [1]. As of 2022, the total number of Chinese airports is 916, of which the number of general aviation airports is 399 and the number of transportation airports is 254, and the total percentage of general aviation airports in the southwest and northwest as well as in Xinjiang is 16%, which is much lower than that in other regions [2]. In contrast, the number of European airports has reached 4,062 as of 2019, and the number of public airports managed by the National Integrated Airport System (NPIAS) in the United States has reached 3,321 as of May 2018 [3]. Therefore, accelerating infrastructure construction remains a key task for China's civil aviation development at this stage [4]. In the future, China's airport construction tasks are mainly focused on the encryption of regional airports in the central and western regions. The central and western regions, especially the mountainous areas in western and southwestern China, have complex and changing terrain conditions, which pose greater challenges for civil airport engineering and construction.

There are many factors affecting the dynamic load characteristics of aircraft landing, in addition to the aircraft's own characteristics, pilot operation, wind speed, but also with the sinking speed, grounding speed, pitch angle, roll angle and other landing state factors and road surface factors such as road surface smoothness, road surface structural dynamics, and other road surface factors are closely related to [5]-[7]. Due to the complexity of the impact contact dynamics of the airframe-landing gear-roadway surface in the landing process, the aircraft landing impact force and its influencing factors and influencing mechanism have not yet been clarified, and the established specifications, as well as the design values of the existing runway bridge project are very different, which makes it difficult to directly guide the engineering practice [8]-[11]. Therefore, facing the national transportation power strategic planning and civil aviation industry infrastructure development needs, for the planning and design of

runway bridges to provide more reasonable and reliable dynamic load parameters, for aircraft landing performance research, as well as aircraft landing impact dynamic loads of this key issue to carry out a systematic study, not only for the airport road surface, especially the new to provide a clear support for the ground load parameters, but also for the safety of the aircraft landing monitoring and assessment of aircraft landing safety is of great significance [12]-[15].

In this study, a spatial attitude and deformation measurement and analysis method based on non-contact measurement technology is proposed for the characteristics and needs of aircraft landing impact test. The method combines theoretical modeling and numerical simulation to construct a complete aircraft landing impact analysis system. By establishing an elastic aircraft dynamics model with a large spreading ratio, the motion characteristics and load transfer mechanism during the landing process are analyzed in depth. At the same time, advanced finite element analysis technology is used to establish a three-dimensional model of an aircraft tire to study the tire deformation and stress distribution law under different landing conditions. Based on the impact spectrum analysis method, the key frequency characteristics of the aircraft landing process are identified, which provides the basis for the anti-impact design of airborne equipment. By comparing and analyzing the safety indexes under different landing parameters, an aircraft landing safety assessment system is established to provide technical support for flight operation and structural design.

II. Aircraft landing characteristics measurement studies

II. A.Kinetic modeling

This paper adopts the method of modal superposition to establish the vibration modal mathematical models of the landing gear system and elastic airframe by taking the elastic airplane with large aspect ratio and the conventional strut-type oil-air cushion landing gear as the objects of study [16].

Taking the large chord ratio elastic airplane body as an example, according to the Lagrange equation, the n-order modal dynamics equations of the elastic airframe considering the structural damping are established.

Large chord ratio elastic aircraft low-order symmetric mode of motion is mainly the wing bending and torsion deformation, the analysis of the right half of the aircraft symmetry model as shown in Figure 1, the establishment of the ground fixed coordinate system $Oxyz$, the origin is located in the center of gravity of the aircraft body at the moment of the tires touching down on the ground, x axis points to the heading position, y axis perpendicular to the plane of symmetry of the body along the spreading of the layout, z axis plumbing downwards.

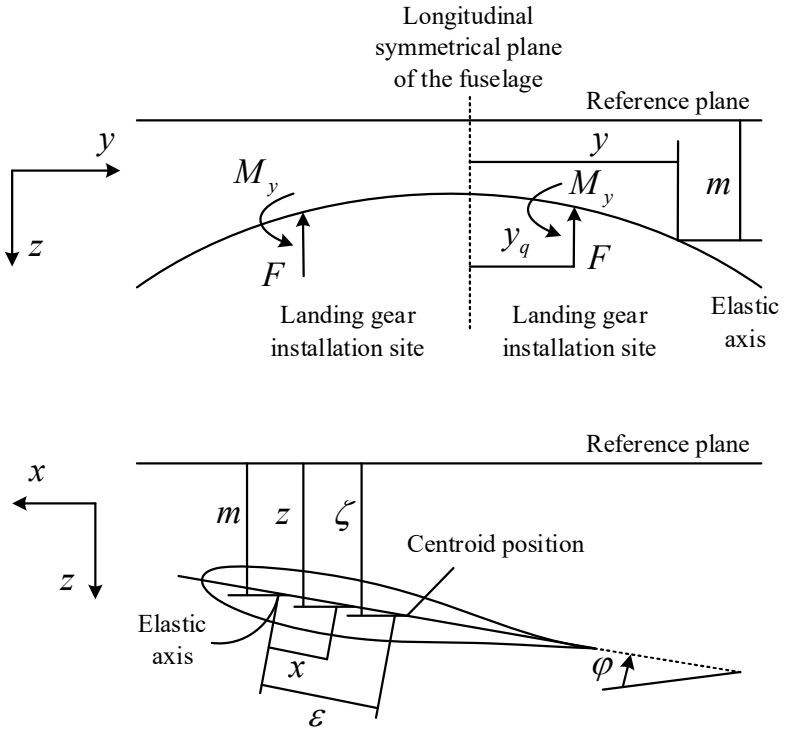

Figure 1: Elastic deformation analysis of the aircraft

The n-order modal dynamics equation for an elastic body considering structural damping is:

$$\begin{aligned} &M_n\ddot{a}_n + M_n\omega_n^2 a_n + 2\mu_n\omega_n M_n\dot{a}_n \\ &= -F\xi_n - \int_0^{b/2} Lz_n dy + g\int_0^{b/2} m\zeta_n dy \end{aligned} \tag{1}$$

where, a_n is the time function modal coordinates, also known as generalized coordinates, and μ_n is the critical damping coefficient of the n th order vibration mode. ω_n is the body elastic vibration frequency. M_n is the modal mass, and $M_n = \sum m_i\zeta_n^2 m$ is the full-machine mass, where m_i is the mass of the body at the i th section. ζ_n is the displacement function at the center of mass of the section, $\zeta_n(y) = w_n(y) + \varepsilon\varphi_n(y)$. The displacement function at any point of the z_n cross-section chord, $z_n(y) = w_n(y) + x\varphi_n(y)$. ξ_n Landing gear mounting point displacement, $\xi_n = w_n + x_f\varphi_n$, where w_n is the longitudinal displacement at the center of section stiffness. ε and x_f are the chordwise position of the center of mass and landing gear mounting point, respectively. φ_n is the cross-section torsional displacement, which can be simplified to neglect the effect of torsional modes. F is the axial force of the landing gear acting on the buffers of the fuselage. L is the lift force.

Take the strut type oil and gas cushion landing gear as the research object, establish the ground fixed coordinate system $Oxyz$ origin is located in the center of the tire grounding moment, each coordinate axis is parallel to the fuselage ground coordinate system respectively, and the differential equation of motion is:

$$M_n\dot{z}_u = F_z - F_v + M_u g \tag{2}$$

where, F_z is the buffer axial force, which can be simplified as the sum of oil damping force F_{zs} and air pressure F_{za}, the oil damping force is:

$$F_{zs} = \begin{cases} C_s\dot{s}^2 & (\dot{s} \geq 0) \\ -C_s\dot{s}^2 & (\dot{s} < 0) \end{cases} \tag{3}$$

where, C, is the oil rate squared damping. s is the buffer stroke.

Air pressure is expressed as:

$$F_{za} = P_{a0}A_a\left(\frac{V_{a0}}{V_{a0} - A_a s}\right)^{\gamma} \tag{4}$$

where, P_{a0} is the initial pressure of the air cavity. A_a is the effective pressure area of the air cavity. V_{a0} is the initial volume of the air cavity. γ is the air cavity compression multivariate index, generally taken as 1.1~1.4.

F_v is the tire support reaction force with:

$$F_v = (1 + C_T\dot{\delta})m_T\delta^T \tag{5}$$

where, C_T is the vertical vibration damping coefficient of the tire, generally taken as 0.04. $m_T\delta^T$ is the function of the static pressure curve of the tire, which can be determined by the tire test. δ is the tire compression, where,

$$\delta = \begin{cases} z_u & (z_u \geq 0) \\ 0 & (z_u < 0) \end{cases} \tag{6}$$

The elastic airplane body dynamics model and the landing gear motion model are integrated to calculate the first-order differential equations of motion for landing an elastic airplane with a large spreading ratio.

In the synchronization phase, the buffer is uncompressed and the initial conditions $\dot{a}(0) = v_0$, $a_0(0) = 0, \dot{a}_1(0) = 0, a_1(0) = 0$, are obtained:

$$\begin{cases} M_0\ddot{a}_0 = -F_z - K_L W_{tot} + M_0 g \\ M_1\ddot{a}_1 + M_1\omega_1^2 a_1 + 2\mu_1\omega_1 M_1\dot{a}_1 = (F_z + K_L W_u)\xi_1 \\ M_u\ddot{z}_u = M_u\ddot{z}_f = M_u(\ddot{a}_0 + \ddot{a}_1\xi_1) = F_z - F_v + M_u g \end{cases} \tag{7}$$

Asynchronous phase, buffer compression, and the end value of the synchronous phase is obtained as the initial value for this phase:

$$\begin{cases} M_0\ddot{a}_0 = -F_z - K_L W_{tot} + M_0 g \\ M_1\ddot{a}_1 + M_1\omega_1^2 a_1 + 2\mu_1\omega_1 M_1\dot{a}_1 = -(F_z + K_L W_u)\dot{\xi}_1 \\ M_u\ddot{z}_u = F_z - F_v + M_u g \end{cases} \tag{8}$$

The following assumptions were taken for the elastic airplane landing dynamics model described above:

(1) The structural deformation of the airplane is described by the quasi-modal method, and the airplane motion is described by the linear vibration theory.

(2) The airplane moves symmetrically, maintaining only its own degrees of freedom in the direction of vertical motion, and that the airplane is zeroed at the moment of the grounding instant.

(3) The main landing gear is mounted vertically to the fuselage.

(4) Changes in aircraft lift due to elastic deformation of the wings are not considered.

(5) The effect of torsional modes is not considered.

II. B.Material properties and selection of aircraft tires

II. B. 1) Fluid Cavity Units

This paper presents a surface-based fluidic cavity cell that can simulate a confined structure filled with gas or liquid. The fluidic cavity cell is used to simulate the air pressure of an aviation tire to reflect the changes in the air pressure inside the tire due to the deformation of the tire during landing.

The boundary of the fluidic cavity is formed by cell-based surfaces, and the normal direction of these cell-based surfaces points towards the interior of the cavity. The finite element model of a surface-based fluid cavity cell is shown in Figure 2. When defining a fluid-cavity cell, a reference point must first be defined with a completely confined surface. When defining the reference point, if the finite element model is axisymmetric or symmetric, then the reference point must be defined at the axis of symmetry shown on the left of Fig. 2, and if the axis of symmetry has an intersection, then the reference point must be the intersection of the axis of symmetry (shown on the right of Fig. 2). If the finite element model is arbitrary, then the reference point is also arbitrary. When defining cell-based surfaces, the defined surface must be completely closed. The air pressure inside the tire can be simulated by means of the relevant properties of the defined fluid-cavity cell.

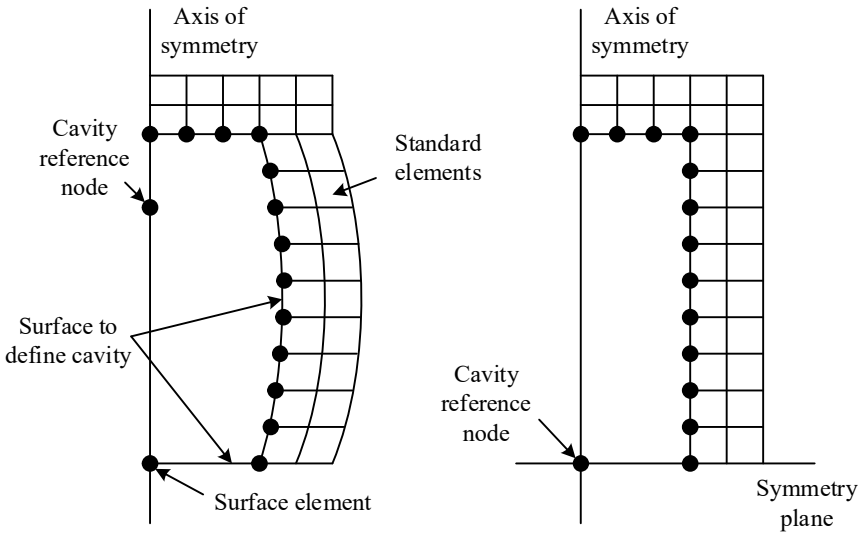

Figure 2: Finite element model based on surface fluid cavity elements

Assuming that the gas filled in the tire is an ideal gas, the equation of state for an ideal gas is:

$$\tilde{p} = \rho R(\theta - \theta^z) \tag{9}$$

where $\tilde{p}$ is the absolute pressure:

$$\tilde{p} = p + p_A \tag{10}$$

p_A is the pressure of the surroundings, p is the pressure inside the cavity, R is the gas constant, θ is the temperature of the environment, θ^z is the absolute zero, and R can also be determined by the universal gas constant $\tilde{R}$ and the mass of the gas molecule MW :

$$R = \frac{\tilde{R}}{MW} \tag{11}$$

The current fluid volume can be expressed as:

$$\bar{V} = \sum \bar{V}^e(p,\theta) = \sum m^e / \rho = m / \rho \tag{12}$$

Then the corresponding volumetric pressure is satisfied:

$$\frac{d\bar{V}}{dp} = -\frac{m}{\rho^2} \cdot \frac{d\rho}{dp} = -\frac{mR(\theta - \theta^z)}{(p + p_A)} \tag{13}$$

That is, when the volume of the cavity changes, the corresponding pressure changes.

Regarding the compressibility of a fluid can be expressed by the bulk modulus of the fluid:

$$p = -K\left(\frac{V - V_0}{V_0}\right) = -K_{\rho R}(\rho^{-1} - \rho_0^{-1})V_0 \tag{14}$$

where p is the current air pressure, K is the fluid bulk modulus, V is the current volume of the fluid, ρ is the density at the current air pressure, ρ_0 is the density at the current temperature when the air pressure is zero, and V_0 is the volume at the initial temperature when the air pressure is zero.

II. B. 2) Material properties of rubber

Rubber, as the main component of aviation tires, the accuracy of its mechanical properties is crucial to the results of transient impact of aviation tires. In this paper, the mechanical properties of the tread rubber of aviation tires are described by a visco-hyperelastic intrinsic model. The mechanical properties of other rubbers are obtained from tire companies and are simulated using linear elasticity, and the relevant parameters of the main rubber materials are shown in Table 1.

Table 1: Air tyre rubber material parameters

	Lining layer	Tyre rubber	Tread	Band rubber	Tyre clamp	Tyre guard
Modulus (MPa)	11	13	10	22	31	45
Poisson ratio	0.499	0.499	0.499	0.499	0.499	0.499
Density kg/m3	1036	1125	1260	1070	1070	1630

II. B. 3) Other material properties

Since beads and hubs are not the focus of this paper, the material properties of both of them are characterized by linear elasticity, with modulus set at 500 GPa, Poisson's ratio at 0.23, and density at 7025 kg/m3.

Regarding the simulation of the reinforcing layer, ABAQUS provides a rebar layer that can simulate the reinforcing layer in the shell, membrane, and surface units, and the rebar layer should be embedded in the parent unit in the modeling project of aviation tires, and the material properties of the rebar layer and the parent unit should be defined separately, and the relative sliding of the rebar layer and the parent unit should not be considered. Sliding. When defining a rebar layer, it is necessary to define its name, the cross-sectional area of each rebar layer and its spacing in the solid cell, the material name of the rebar, and the orientation angle.

II. C.Establishment and validation of 3D finite element model of aviation tire

II. C. 1) Tire finite element modeling

First of all, the material distribution map of the aviation tire is obtained, imported into AutoCAD software, and then meshed, in which the quadrilateral cells are kept as square as possible, and the triangular cells are as close as possible to the square triangles. After completing the above work, the node information of the mesh is imported into a DXF file, and then the DXF file is imported into TYABAS software, which is a special software for tire analysis developed in the laboratory, and the mesh is adjusted and the relevant attributes are given to the finite element model in TYABAS software. Finally, the INP file, which can be directly analyzed by ABAQUS, was exported and the

INP file was imported into ABAQUS to obtain the finite element model of the 2D cross-section diagram of the aviation tire. Then the rim diagram is imported into ABAQUS and the interaction between the tire finite element model and the rim finite element model is defined, thus obtaining the 2D finite element model of the aviation tire. The 3D model of the tire must be used for analysis in performing later work, so in this paper, the 2D finite element model is rotated using the SYMMETRIC MODEL GENERATION command to obtain the 3D finite element model of the aviation tire [17].

II. C. 2) Finite element modeling of transient shocks

In this paper, ABAQUS finite element analysis software has been used to perform a finite element analysis of an aerial tire falling at a certain height and impacting a rigid ground [18]. In this case, the load is applied to the center reference point of the tire, and then the reference point is coupled to the surface on the inside of the rim, a predefined velocity field perpendicular to the ground is applied to the tire, the road surface is defined in terms of a rigid plane and the six degrees of freedom of the road surface are fixed, and the contact between the tire and the ground surface is defined as a surface-to-surface contact based on a penalty function. The above process is mainly accomplished by modifying the INP file. In addition, the initial velocity of the aerial tire and the load it is subjected to can be changed by modifying the INP file. The effect of gravity is considered throughout the impact analysis, and the acceleration of gravity is set to 9820 mm/s2. Regarding the application of loads, in static analysis, they are usually applied in the form of concentrated forces. However, in the dynamic analysis, the inertia of the mass must be taken into account, and the load is applied in the form of concentrated mass. In order to investigate the difference between the dynamic response of the two forms of load application and to determine the specific form of load to be applied in the transient impact response analysis of an aircraft tire.

III. Tyre landing impact deformation and stress analysis

III. A. Aircraft Landing Impact Data Analysis

III. A. 1) Principles of selecting parameters for analyzing shock spectra

When collecting shock signals and selecting data segments for analysis, the following points need to be noted:

(1) Data start point: assuming that the initial conditions are zero, so in the selection of impact data segment needs to ensure that the starting part is in the unimpact, or the value of the part is close to zero.

(2) Data cut-off point: sampling cut-off data should meet the end of the data peak value is less than 30% of the peak value of the signal. As for the length of the signal, you need to consider the scope of the analyzed frequency band, if the shock vibration frequency that is high-frequency, and low-frequency, in order to get the maximum spectrum of the impact, you need to select a longer signal segment.

(3) The choice of sampling rate: for the calculation of the impact spectrum, select the appropriate sampling rate is not only to eliminate frequency confusion, but also with the calculation error. Generally speaking, the sampling rate shall not be lower than 4 times the upper limit of the analyzing frequency, and it is better to choose 6~10 times.

(4) Analysis of frequency point selection: in order to save computational workload can not be used to select the point of equal frequency spacing, and the use of 1/12 octave, practice has proved that 1/12 octave frequency point distribution can meet the requirements of the analysis of the impact of the landing of the aircraft.

III. A. 2) Aircraft landing impact spectrum analysis

The time-domain shock signal at the moment of aircraft landing is shown in Fig. 3, and (a) and (b) represent the landing shock waveform and response spectrum, respectively. The curve trend is similar to the vibration resonance curve, the acceleration amplification coefficient is larger in 450~550Hz, and the maximum value of 6.2 occurs in 507Hz.By the definition of the impact spectrum, the self-oscillation frequency of the aircraft on-board equipment and external components should be avoided to appear in the frequency range, and if the landing in the region should be taken to damping anti-shock design, in order to minimize the damage caused by the impact environment on the equipment.

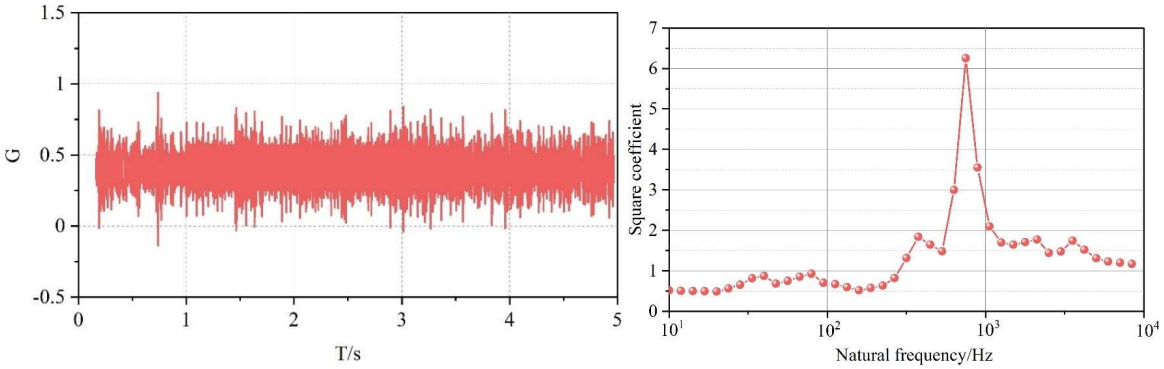

(a) Landing shock wave (b) Landing impact response spectrum

Figure 3: Time domain impact signal of aircraft landing moment

III. B. Deformation and Stress Analysis under Different Landing Loads

III. B. 1) Section Profile and Grounding Characteristics

The section profile indicators corresponding to different landing loads are shown in Table 2. The landing load F, compression amount $y_{2\_\max}$, compression rate $\lambda_{\max}$, compression amount $\delta_{\max}$, compression ratio $\lambda_{\max}\_\delta$, and cross-section width W_F 6 section profile indexes are analyzed, and it can be seen that the section profiles corresponding to different landing loads differ greatly. The difference between the compression amount and compression rate calculated by the kinetic model and finite element simulation is small when the landing load is 111094N and 146275N, and the difference between the two increases when the landing load is 185675N, 228200N and 273160N respectively, but the overall difference is still within the acceptable range, and the compression rate corresponding to the impact load of 228200N and 273160N is close to or exceeds the permissible range for aviation tires. The compression ratio corresponding to the impact loads of 228200N and 273160N is close to or exceeds the permissible compression ratio of aviation tires. Therefore, in the normal range of use, this paper reduces the tire to a linear elastic spring model still has a high degree of accuracy.

Table 2: The corresponding profile of the different landing load

F (N)	$y_{2\_\max}$ (mm)	$\lambda_{\max}$ (%)	$\delta_{\max}$ (mm)	$\lambda_{\max}\_\delta$ (%)	W_F (mm)
111094	53.89	18.25	57.98	19.63	428.25
146275	70.9	24.03	70.29	23.82	439.92
185675	89.99	30.5	83.51	28.29	451.67
228200	110.61	37.46	97.56	33.06	463.14
273160	132.41	44.86	112.62	38.16	474.05

Table 3 shows the grounding characteristics corresponding to different landing loads. The four grounding characteristic indexes of landing load F, ground contact area $Area$, average ground pressure F_{mean} and rectangular coefficient C_{rec} were analyzed, and it can be seen that each index increases with the increase of land load, in which the proportion of ground contact area changes with land load is larger, and the proportion of average ground pressure and rectangular coefficient change with land load is relatively small.

Table 3: The earthing characteristics of different landing loads

F (N)	$Area$ (mm2)	F_{mean} (Mpa)	C_{rec}
111115	73914	1.5171	0.665
146295	93475	1.5609	0.7327
185695	111289	1.6682	0.7657
228220	128048	1.791	0.8131
273180	148169	1.8461	0.8183

In summary, the landing load has a more obvious effect on both the section profile and grounding marks, and when the landing load changes, the compression rate and grounding area caused by the degree of change is also

larger. In the process of aviation tire research and development, it is necessary to carry out strict design and testing in accordance with the aircraft type it serves. In the actual use of the process, must make the aviation tire in its calibration load range work, shall not exceed the standard overload.

III. B. 2) Skeleton material stress distribution

During the landing impact of an aircraft tire, the stress distribution pattern of each cord in the grounded section is significantly different from that in the static inflated condition, and the stress values are generally smaller in the grounded region. The -90° section past the highest point of the tire crown (hereafter referred to as the highest section) may have relatively large stress values due to expansion and stretching, which can be contrasted with the stress distribution in the grounded section. Therefore, the stress distribution patterns of some cords in the grounded section and the highest section were extracted to summarize the effect of landing load on the stress distribution of the skeleton material. The cords with more representative stress distributions are selected as the research objects here.

The stress distribution pattern of the carcass cords under different landing loads is shown in Fig. 4, with (a) and (b) indicating the stress distribution in the grounded section and the highest section, respectively. Under different landing loads, the stress distribution curves of each carcass cord in the highest section almost completely overlap, but still show the relatively higher position of the stress curve when subjected to larger landing loads. The overall behavior of each carcass cord shows that the larger the landing load is, the more drastic the change of the stress curve is. The fluctuation of the stress distribution curve of each tire cord in the figure is more violent, so in the process of actual R&D and design, extra attention should be paid to the structural safety of each peak position in the figure.

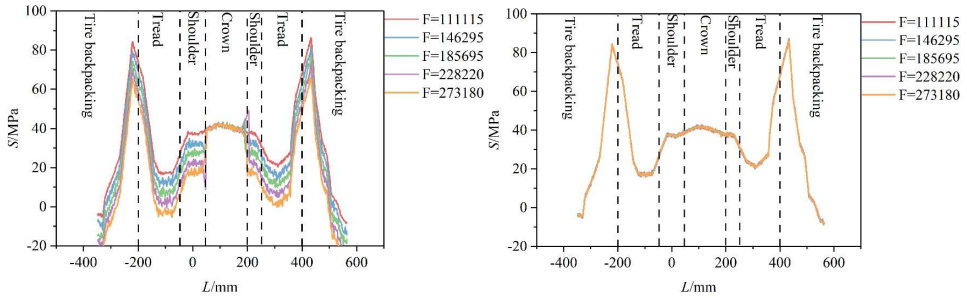

(a) Stress distribution of ground (b) Stress distribution of maximum section

Figure 4: Stress distribution under different landing loads

The stress distribution patterns of the bundled cords under different landing loads are shown in Fig. 5, with (a) and (b) indicating the stress distribution at the grounded section and the highest section, respectively. With the increase of the landing load, the stress curves of all the bundled cords show a general downward trend. In the highest section, the distance between the stress curves of each cord is small, and the effect of landing load on the stress distribution characteristics of each cord in the highest section is not very significant. In the grounded section, the stress extremes of each cord under different landing loads are more different. The overall trend of the stress distribution of each cord shows a decrease with the increase of the landing load, so when the landing load increases, it may not affect the tensile safety of the bundled cord.

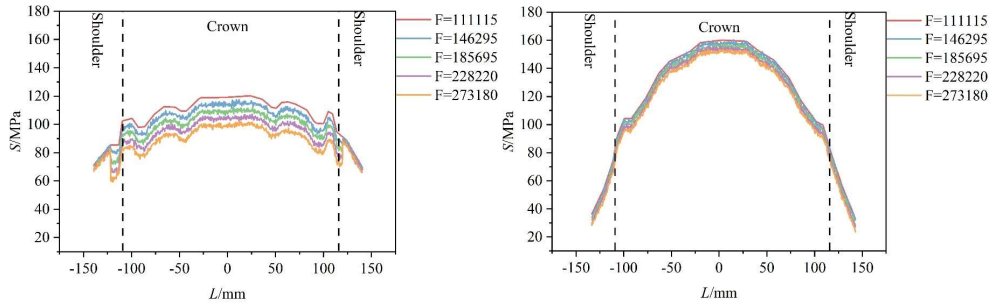

(a) Stress distribution of ground (b) Stress distribution of maximum section

Figure 5: Stress distribution under different landing loads with beam curtain lines

In summary, the landing load has different effects on the carcass cord and the belt bundle cord, in the highest section, the carcass cord stress value increases with the increase of the land load, and the belt bundle cord stress value decreases with the increase of the land load, but the effect is not very significant. In the grounded section, each carcass cord stress curve generally shows a trend of becoming steeper and fluctuating more sharply with the increase of land load, while each belt cord stress curve generally shows a trend of flattening with the increase of land load, but the belt cord stress curve at the end point of the tire shoulder shows an upward trend, and the trend may be steeper.

III. C. Security analysis

In this paper, two indicators, contact force and deformation, will be used to analyze the safety of aviation tires. Each aircraft type has a corresponding safe landing speed, so the speed of each landing will be different. In this paper, it is assumed that the forward speed of the aircraft is maintained at 73.5 m/s during landing, and the safety of the tires is analyzed when the sink rate of the aircraft is 1.0, 2.0, and 2.5 m/s, respectively.

The variation curves of tread pressure of aviation tires at different aircraft sink rates are shown in Fig. 6. It can be seen that the tread pressure increases as the aircraft sink rate increases. When the sink rate of the aircraft is 1.0m/s, the tread pressure reaches a peak value of 4.62MPa after 0.05s, and then reaches a stable state in 0.22s. When the sink rate reaches 2.0m/s, the tread pressure increases rapidly and reaches a peak value of 9.19MPa after 0.05s, and then another peak value of 8.9MPa reappears at 0.1s, which is mainly due to the interaction between the landing gear and the tires after the aircraft touches the road surface. When the sink rate is 2.5m/s, a peak value of 13.41MPa is reached after 0.05s, after which a steady state is reached at 0.27s.

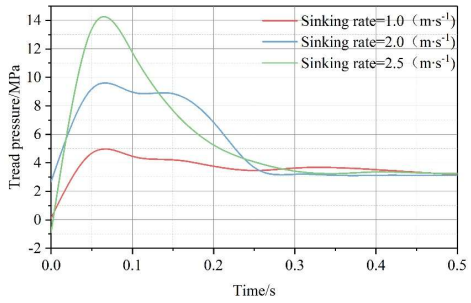

Figure 6: Tread pressure of the tire under different sink rates

The variation curves of the contact force of aviation tires at different sink rates are shown in Fig. 7. It can be seen that the contact force of the tire increases gradually with the increase of the sinking rate of the aircraft. The maximum load that the aviation tire can withstand is 379636 N. When the sink rate of the aircraft is 1.0 m/s, the tire contact force reaches a peak value of 325460 N after 0.07 s. When the sink rate is 2.0 m/s, the contact force from the tire contacting the airport road surface reaches a peak value of 481,121 N after 0.1 s, which is more than the range of the tire to withstand, and then the contact force decreases rapidly after the tire and the landing gear absorbs the impact energy of the aircraft. After the tires and landing gear absorbed the impact energy of the aircraft, the contact force of the tires decreased rapidly. When the sink rate is 2.5m/s, the contact force reaches a peak value of 563522N after 0.10s, and then returns to a stable state. Therefore, when the sink rate of the aircraft is 2.0m/s, the aviation tires can be used safely without affecting the safe landing of the aircraft, but as the sink rate of the aircraft increases the contact force of the tires exceeds its maximum load, there will be a risk of tire blowout.

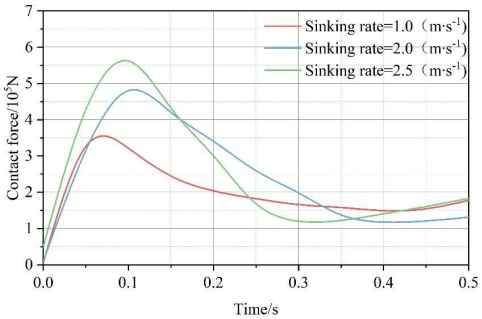

Figure 7: Contact force of the tire under different sink rates

The variation curves of aviation tire deformation under different aircraft sink rates are shown in Fig. 8. It can be seen that the tire deformation gradually increases with the increase of sink rate. From the formula of aviation tire sink rate, it can be seen that the rated deformation of aviation tire is 0.166 m. When the aircraft sink rate is 1.0 m/s, the deformation of the tire reaches the peak value of 0.092 m after 0.05 s. When the sink rate is 2.0 m/s, the deformation of the tire reaches the maximum value of 0.136 m after 0.1 s, and then reaches a stable state. When the sinking rate is 2.5m/s, the deformation of the tire is 0.154m which is within the safe range. As the sink rate of the aircraft increases, the contact force and deformation of the aviation tires also increase. If these values exceed the rated value of the tire, the tire cord ply may suffer structural damage, and the structure of the tire may be damaged, which may lead to the risk of a blowout.

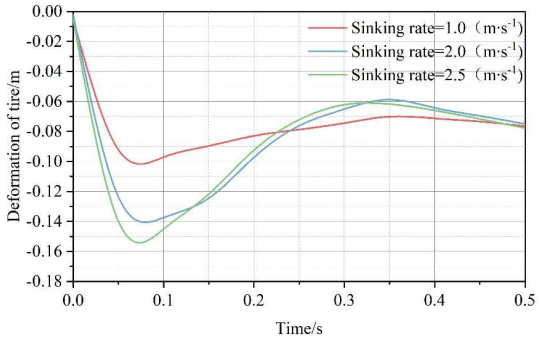

Figure 8: Deformation of the tire under different sink rates

In summary, when the aviation tires simultaneously satisfy the contact force and the deformation amount within the safety range, the aircraft can land safely under the aircraft sink rate of 1.0 m/s. The landing gear buffer and tire show high nonlinearity during the motion process, while the landing gear in the simulation experiment of this paper is simplified as a linear elastic element with damping, and the material and tire pressure of the aviation tire are also simplified, which leads to a certain deviation of the calculation results from the actual.

IV. Conclusion

In this paper, the deformation characteristics and stress distribution law during the landing impact of aircraft are analyzed in depth by establishing the elastic aircraft dynamics model with large chord ratio and the three-dimensional finite element model of aviation tires. It is found that the landing load has a significant effect on the tire section profile and grounding characteristics, and when the landing load increases from 111094N to 228200N, the tire compression rate increases from 18.25% to 37.46%, and the grounding area expands from 73914mm² to 128048mm². The impact spectrum analysis showed that the aircraft landing impact signal exhibited a high acceleration amplification coefficient in the frequency band of 450-550 Hz, and the self-oscillation frequency of the airborne equipment should be avoided to fall within this frequency band.

The stress analysis of the skeleton material shows that the carcass cords and belt cords exhibit different stress distribution patterns under different landing loads. In the highest section, the stress value of the carcass cord shows an increasing trend, while the stress value of the belt cord decreases relatively. In the grounded section, the stress curve of the tire cord changes more drastically, while the stress distribution of the belt cord tends to flatten.

The safety analysis results show that the aircraft sink rate directly affects the contact force and deformation of the tire. When the sink rate is 1.0m/s, the peak contact force of the tire is 325460N, and the deformation is 0.092m, which are within the safety range. When the sink rate increased to 2.0m/s, the peak contact force reached 481121N, which exceeded the maximum load of 379636N of the tires, and there was a potential safety hazard. This study provides an effective measurement and analysis method for the aircraft landing impact test, which has important engineering application value for improving the safety of aircraft landing and optimizing the structural design.

Funding

This project is supported by Chinese Aviation Science Foundation: Application of Artificial Intelligence in Landing Gear Dynamics (No.2023M009023006).

References

[1] Zhu, Y., Jia, M., & Shi, Y. (2017). Analysis on Current Development Situations, the Key Issues and Countermeasures of China's General Aviation Industry. Procedia Engineering, 174, 871-877.

[2] Han, B., Wang, L., Deng, Z., Shi, Y., & Yu, J. (2022). Source emission and attribution of a large airport in Central China. Science of the Total Environment, 829, 154519.
[3] Park, J. W., Roh, S., Jang, H., & Seo, Y. J. (2023). The performance of major airports in the Europe, North America and Asia. Asia Pacific Journal of Marketing and Logistics, 35(11), 2808-2833.
[4] He, P., & Sun, R. (2023). Trends and characteristics of incidents in China civil aviation: 1994–2020. Transportation research record, 2677(5), 420-431.
[5] Wong, J., Ryan, L., & Kim, I. Y. (2018). Design optimization of aircraft landing gear assembly under dynamic loading. Structural and Multidisciplinary Optimization, 57, 1357-1375.
[6] Suresh, P. S., Sura, N. K., Shankar, K., & Radhakrishnan, G. (2023). Synthesis of landing dynamics on land-base high performance aircraft considering multi-variate landing conditions. Mechanics Based Design of Structures and Machines, 51(7), 3945-3964.
[7] Liu, G. G., Pei, L. Y., Feng, L., & Wu, Z. W. (2024). A Mathematical Model for Dynamic Vibration Analysis of a Landing Aircraft. Journal of Vibration Engineering & Technologies, 12(3), 4149-4162.
[8] Bronstein, M., Feldman, E., Vescovini, R., & Bisagni, C. (2015). Assessment of dynamic effects on aircraft design loads: The landing impact case. Progress in Aerospace Sciences, 78, 131-139.
[9] Hou, X., Xue, P., Wang, Y., Cao, P., & Tang, T. (2018). Theoretical and discrete element simulation studies of aircraft landing impact. Journal of the Brazilian Society of Mechanical Sciences and Engineering, 40(3), 115.
[10] Liu, W., Wang, Y., & Ji, Y. (2023). Landing Impact Load Analysis and Validation of a Civil Aircraft Nose Landing Gear. Aerospace, 10(11), 953.
[11] Wang, H., Wu, D., Wang, F., & Ren, H. (2018). A method for determining the horizontal impact load based on the rotational speed of the aircraft's wheel in a landing gear drop test. International journal of crashworthiness, 23(6), 627-634.
[12] Pytka, J., Budzyński, P., Łyszczyk, T., Józwik, J., Michałowska, J., Tofil, A., ... & Laskowski, J. (2019). Determining wheel forces and moments on aircraft landing gear with a dynamometer sensor. Sensors, 20(1), 227.
[13] Hameed, A., Zubair, O., Shams, T. A., Mehmood, Z., & Javed, A. (2020). Failure analysis of a broken support strut of an aircraft landing gear. Engineering Failure Analysis, 117, 104847.
[14] Castrichini, A., Cooper, J. E., Benoit, T., & Lemmens, Y. (2018). Gust and ground loads integration for aircraft landing loads prediction. Journal of Aircraft, 55(1), 184-194.
[15] Lee, K. B., Jeong, S. H., Cho, J. Y., Kim, J. H., & Park, C. Y. (2015). Hard-landing simulation by a hierarchical aircraft landing model and an extended inertia relief technique. International Journal of Aeronautical and Space Sciences, 16(3), 394-406.
[16] Feng Song,Zhang Guiyong,Wan Decheng,Jiang Shengchao, Sun Zhe & Zong Zhi. (2021). On the treatment of hydroelastic slamming by coupling boundary element method and modal superposition method.Applied Ocean Research,112,
[17] Dimitrienko Yuriy,Koryakov Mikhail,Yurin Yuriy,Sborshchikov Sergey & Bogdanov Ilya. (2023). Finite element modeling of thermal stresses in aerospace structures from polymer composite materials. E3S Web of Conferences,376,01033-01033.
[18] Li H.,O'Hara P. & Duarte C.A.. (2021). Non-intrusive coupling of a 3-D Generalized Finite Element Method and Abaqus for the multiscale analysis of localized defects and structural features. Finite Elements in Analysis & Design,193.